Materials Today Advances 13 (2022) 100196

Contents lists available at ScienceDirect

Materials Today Advances

journal homepage: www.journals.elsevier.com/materials-today-advances/

Early stages of liquid-metal embrittlement in an advanced high-strength steel

Y. Ikeda [a, b], R. Yuan [a], A. Chakraborty [c], H. Ghassemi-Armaki [d], J.M. Zuo [a], R. Maaß [a, b, *]

[a] Department of Materials Science and Engineering, University of Illinois at Urbana-Champaign, Urbana, IL, 61801, USA
[b] Federal Institute of Materials Research and Testing (BAM), Unter den Eichen 87, 12205, Berlin, Germany
[c] ArcelorMittal Global Research and Development, East Chicago, IN, 46312, USA
[d] General Motors R&D, Manufacturing Systems Research Laboratory, Warren, MI, 48092, USA

ARTICLE INFO

Article history:
Received 5 October 2021
Received in revised form
1 December 2021
Accepted 1 December 2021
Available online xxx

Keywords:
Advanced high strength steels
Liquid metal embrittlement
Transmission electron microscopy
4-Dimensional scanning transmission electron microscopy

ABSTRACT

Grain-boundary degradation via liquid-metal embrittlement (LME) is a prominent and long-standing failure process in next generation advanced high-strength steels. Here we reveal, well ahead of the crack tip, the presences of nano-scale grains of intermetallic phases in Zn-infiltrated but uncracked grain boundaries with scanning- and 4D transmission electron microscopy. Instead of the often-reported Zn-rich Fe-Zn intermetallics, the nano-scale phase in the uncracked infiltrated grain boundaries is identified as the Γ-phase, and its presence reveals the local enhancement of strain heterogeneities in the grain boundary network. Based on these observations, we argue that intermetallic phase formation is not occurring after cracking and subsequent liquid Zn infiltration but is instead one of the primary nano-scopic drivers for grain-boundary weakening and crack initiation. These findings shift the focus of LME from micro- and meso-scale crack investigations to the very early stages immediately following Zn diffusion, after which secondary phase nucleation and growth emerge as the root-cause for failure.

1. Introduction

Our societal need for high-performance structural materials, combined with today's increasing demand for energy efficiency, continuously promotes the discovery and development of new complex technological alloys. Specifically, in the area of iron-based alloys, notably steels, advanced high strength steels (AHSS) of the third generation are now on the horizon. Besides the best combination between strength and ductility, these widely used alloys require additional optimizations for applications in light-weight structures or harsh environments. To this end, their strength-to-weight ratio [1], and their corrosion resistance [2] have been in the focus of alloy design. The particular requirement of an excellent corrosion resistance of AHSS is often met via the application of Zinc (Zn)-based coatings that are applied through an industrially viable continuous galvanizing route.

Whilst galvanizing significantly improves the corrosion resistance of AHSS, a major drawback is the low melting point of Zinc that during typical joining operations, such as resistance spot welding (RSW), forms a molten surface layer in the heat-affected zone of the process zone at the shoulder or periphery regions of the weld [3,4]. Even though the liquid Zn only covers the solid substrate for a fraction of a second, it has become evident that it promotes embrittlement, thereby representing a case of the known but fundamentally not equally well understood liquid-metal embrittlement (LME) phenomenon [5–7].

Most generally, LME can occur when a liquid metal (or alloy) is in contact with a solid metal (alloy) in the presence of an external tensile stress. During the coexistence of the liquid and the solid, grain-boundary weakening of the solid substrate may proceeds via penetration of the liquid phase. Consequently, local intergranular micro-cracking might be triggered under the complex stress states present during most joining processes [6,8,9], followed by further infiltration of the liquid metal, which in the case of galvanized AHSS is Zn. These microscopic processes lead to a significant degeneration of joined-galvanized AHSS components and represent a fundamental problem of structural integrity [8,10–12].

Material systems that are known to suffer from LME of grain boundaries are, for example, Ni-Bi [13], Al-Ga [14–17], Al-Hg [18], and Ti-H [19], and various phenomenological descriptions of the

* Corresponding author. Department of Materials Science and Engineering, University of Illinois at Urbana-Champaign, Urbana, IL, 61801, USA.
E-mail address: robert.maass@bam.de (R. Maaß).

https://doi.org/10.1016/j.mtadv.2021.100196

underlying mechanisms have been proposed. In the case of the here considered galvanized AHSS, represented by the Fe-Zn binary, only limited detailed microstructural insights are available. However, the general steps of how LME proceeds, are believed to be the same. These steps can be summarized as follows [6,8,11,20–25]: i) stress-assisted accelerated diffusion of the liquid species into the solid substrate along the grain-boundary network [8,11,20–22,26], ii) cracking along infiltrated grain-boundaries [8,20,21,23–25], iii) crack filling with the liquid metal [8,20–25], and iv) continued grain-boundary infiltration ahead of the crack tip [20,22,24,25]. Importantly, the formation of intermetallic phases often observed in LME-cracks is said to occur *during* steps iii) and iv) and is thus not the critically weakening step in the degradation process [6,8,11,21,23–25,27]. Instead, recent studies proposed that grain-boundary decohesion is caused by chemical effects that alter the atomic-binding strength [7,22,28]. In the present study, we provide evidence for nanoscale intermetallic phase nucleation occurring in Zn-infiltrated but uncracked boundaries far ahead of the crack tip that revise the commonly presented mechanistic sequence.

The above quoted sequence of events does not specifically address the origin of grain-boundary weakening, nor does it further specify the mechanistic details of how cracking proceeds. For example, what causes the high diffusivity of the molten species? Why are some grain-boundaries prone to infiltration and/or cracking and others not? Is interfacial weakening solely due to the presence of the infiltrating species, or is the formation of secondary phases critical? These fundamental questions have been central to the community for decades and demand for detailed atomic- and nanoscale microstructural investigations to understand LME in AHSS. Here, we aim at addressing the third of the afore posed questions.

In contrast to the Al-Ga [14–17] and Al-Hg [18] systems that show embrittlement at ambient conditions, the fundamental questions of LME are even more challenging to answer for the Fe-Zn system due to the high temperature of the ductility trough (700–900 °C) [6] and the high vapor pressure of Zn [29], prohibiting in-situ investigations at high enough spatial resolution (e.g. electron microscopy). Furthermore, LME of galvanized AHSS is often linked to sub-second processing steps and coexistence times of the solid substrate and liquid Zn-phase, making direct observations at the microstructural scale very difficult. These hurdles in combination with the strong industrial interest have directed focus on either effects of processing parameters, such as weld pressure and current [30–32], or on post-mortem analysis of cracked regions [8–10,12,20,22–25,27,33], which reveal rather mesoscale microstructural changes after cracking with a primary focus on Zn-infiltrated cracks.

To shed a more detailed light onto the early stages of LME crack formation and the related nanoscopic microstructural changes in the Fe-Zn system, we follow here the strategy of finding and characterizing Zn-infiltrated but uncracked grain boundaries. The approach reveals evidence for that the nucleation of intermetallic phases and their subsequent growth may be the root cause of local grain-boundary decohesion, which would constitute an alternative origin than hereto discussed in the literature.

2. Materials and methods

We investigate an industrially produced 1.4 mm thick third-generation galvanized AHSS [containing a maximum of 0.26 wt% C, 2.0 wt%Si, 2.3 wt%Mn, 0.04 wt%P, 0.01 wt%S, 1.0 wt%Al, 0.2 wt%Cu, 0.005 wt%B, 0.15 wt%(Ti + Nb), and 0.6 wt%(Cr + Mo)] sheet-material having a tensile strength of more than 1 GPa. The AHSS was annealed in N_2-5%H_2 atmosphere containing a partial pressure, pO_2, of 2.52×10^{-21} atm, followed by galvanization in a Zn-0.2 wt% Al bath, which produced a ~9 μm thick GI-coating on top of the steel containing ferrite, martensite, bainite, and small amounts of retained austenite. The GI-AHSS was resistance spot welded in a three-layer stack assembly, where the top sheet was the GI-AHSS, followed by two 1.5 mm thick sheets of galvanized extra deep drawing steel (EDDS, containing 0.002C, 0.08Mn, 0.10P, 0.005S, 0.005Si, 0.017Cu – all in wt%). RSW was carried out using a 75/85kVA Taylor-Winfield RSW instrument with a 6 mm diameter copper electrode. The welding condition was chosen according to the SEP1220-2 guidelines [34]. During RSW, a constant electrode force of 4.5 kN and current of 9.2 kA were applied. This welding current is just below expulsion, corresponding to the highest current for achieving a maximum nugget size. The duration of the welding squeeze, weld, and hold time were 1167, 383 and 300 ms, respectively. A cross section sample was prepared by using low speed sawing, such that a 3 mm wide, 4 mm thick, and 30 mm long strip centered around the weld spot was obtained. After mechanical polishing, chemo-mechanical polishing with colloidal silica was conducted to minimize possible residual surface damage. In the following sections, we will focus on the Zn infiltrated cracks as well as uncracked Zn infiltrated grain boundaries, all of which are present in the galvanized side of the AHSS. Microstructural details of the EDDS will therefore be omitted in the following. Microstructural characterization was carried out using a JEOL 7000F scanning electron microscopy (SEM) with an energy-dispersion X-ray spectrometer (EDS), a JEOL 20210 LaB6 transmission electron microscopy (TEM), and a JEOL 2200 FS scanning transmission electron microscopy (STEM) equipped with a CEOS probe Cs-corrector and EDS. Furthermore, scanning electron nano diffraction was performed by using an FEI Themis Z Advanced Probe Aberration Corrected Analytical STEM with a precision of 0.2% and a spatial resolution of 1.8 nm. TEM specimens were prepared by using FEI Scios 2 focused ion beam (FIB) via a lift-out method such that samples with an in-plane and out-of plane orientation of the cross-sectional view were obtained. TEM specimens displaying cracked environments were extracted as a cross-section and provide a view along the crack direction upon imaging with TEM. These cracked microstructures were typically located about 10–15 μm away from the crack tip. Uncracked grain-boundary environments were sampled with an in-plane TEM specimen geometry, where the Zn-infiltrated boundary is viewed edge on (in the plane of the cross-sectional cut of the bulk sample), that is in the plane. These uncracked environments were either located at the crack tip, or at the Zn-infiltration front identified ahead of a crack tip.

3. Results and discussion

Fig. 1a displays the cross-sectional view of the spot-welded sample, where an electrode indentation region and a peripheral region are indicated. These regions distinguish themselves through the significantly different LME crack sizes. Cracks under the electrode position are several tens of micrometers long and lack significant Zn infiltration, whereas the cracks located in the here targeted peripheral region are at most 25 μm in length and essentially filled with Zn (Fig. 1b). These smaller and infiltrated cracks have been studied intensely on cross-sectional views and are sought to promote LME-induced failure by intergranular crack propagation [6,8,20–25,27,33]. The backscattered electron (BSE) contrast of Fig. 1b highlights a region enclosed with a dashed rectangle that shows a slightly brighter contrast typically located several hundred nanometers to several micrometers away from the main crack. EDS mapping of this and other similar regions reveals an enrichment of Zn, as shown in the inset of Fig. 1b. That means, Zn has diffused away from the main crack into the surrounding uncracked grain-boundary network. As will become apparent in the

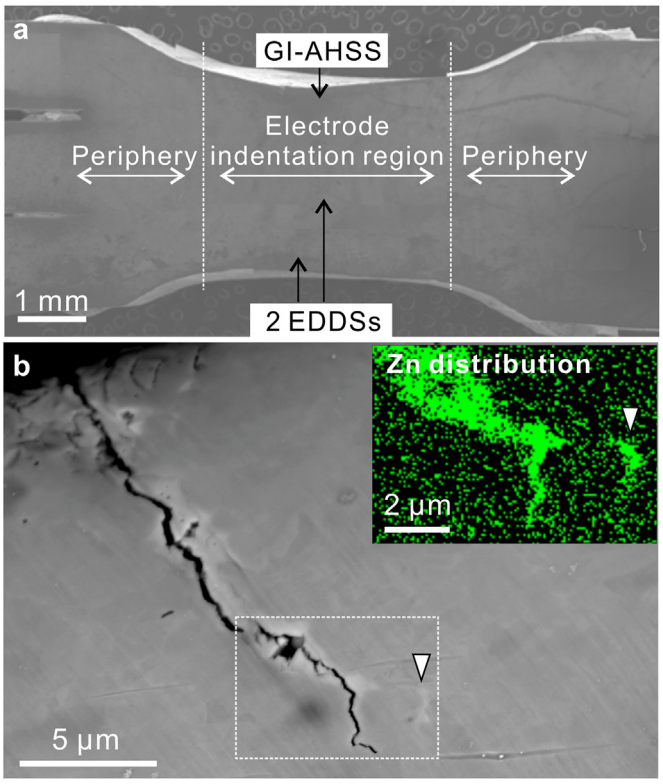

Fig. 1. Cross-sectional SEM micrographs of the spot-welded GI-AHSS steel. a) Cross-sectional overview of the sample (secondary electron contrast). The GI-AHSS is located on top of two EDDS. b) Cross-sectional back-scatter electron image of an LME crack observed at the weld periphery. An arrow inside the dashed box indicates Zn enrichment, which is supported with an EDS map (inset) of the same enclosed area.

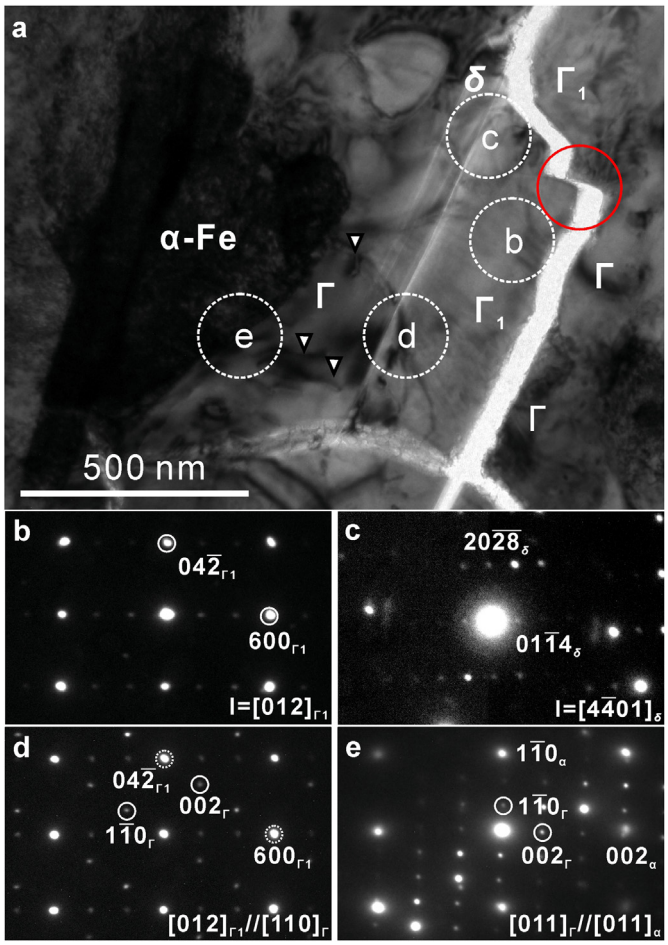

Fig. 2. TEM micrographs of a cracked boundary. a) a BF image of the microstructure along with the cracking path. As indicated, Fe-Zn intermetallic phase-formation is observed. Note that the crack deflection occurred at the interface between the δ- and Γ_1-phase as indicated by the red circle. Dislocations in the Γ-phase are indicated with white arrows. b) to e) selected area diffraction patterns obtained from the regions marked with white circles in a). (For interpretation of the references to color in this figure legend, the reader is referred to the Web version of this article.)

following, Zn-containing regions of uncracked grain boundaries, as indicted in Fig. 1b, are intermetallic phases and not pockets of pure elementary Zn. We note that similar to earlier work, all in the following shown data originates from a 2D projection of an inherently 3D problem. In the following, we will primarily consider grain-boundary environments that contain traces of Zn but that otherwise do not show any immediate decohesion.

Before turning our attention to such uncracked but infiltrated boundaries that reflect microstructural features present during the early stages of LME, we used bright-field (BF) TEM to characterize the present phases in an infiltrated and cracked region. Fig. 2a shows such a crack together with selected area diffraction (SAD) patterns that were taken from the locations b-e indicated in Fig. 2a. The corresponding SAD patterns are displayed in Fig. 2b–e. Independent of the SAD patterns, it is evident from the crack path that it propagates along grain or phase boundaries.

Based on the analysis of the SAD data of Fig. 2 b-e, it can be concluded that the crack propagates entirely in-between intermetallic Fe-Zn phases, including the Fe_3Zn_{10} (Γ) ($I\bar{4}3m$) [35], $Fe_{22}Zn_{78}$ (Γ_1) ($F\bar{4}3m$) [36], and $Fe_{13}Zn_{126}$ (δ) ($P6_3/mmc$) phases [35,37]. In addition, lattice correspondence between Γ/ $\alpha-$ Fe, and Γ/ Γ_1 is revealed (Fig. 2d and e). The obtained orientation relationships are $\langle 012\rangle_{\Gamma_1}$// $\langle 011\rangle_{\Gamma}$ and $\langle 011\rangle_{\Gamma}$// $\langle 011\rangle_{\alpha-Fe}$, respectively, of which the latter indicates a cube-on-cube orientation relationship. Whilst these orientation relationships also have been observed in the microstructure at the interface between the GI coating and the AHSS substrate [38,39], we emphasize that the data of Fig. 2 does not stem from the coating-substrate interface. These findings demonstrate that the Fe-Zn intermetallic phases were first formed, after which the LME crack propagated along the grain boundary at intermetallic grain or phase boundaries. As can be seen from Fig. 2a, the crack predominantly follows phase boundaries between δ/Γ and Γ /Γ_1 and a deflection occurs at the δ/Γ_1 interface, which is indicated with a red circle. Pure Zn was not observed in any of the examined cracked regions.

An additional feature of interest in Fig. 2a is the presence of dislocations inside the Γ-phase, which indicates plastic deformation. Examples are highlighted with small white arrows in Fig. 2a. We note that both the Γ- and the δ-phase have recently been shown to admit micron-scale plasticity at room temperature [40], whereas earlier work limited macroscale plastic flow of Fe_3Zn_{10} to a temperature above 300 °C [41]. Both these reports demonstrate that local stress relaxation via plastic deformation at temperatures well below the welding temperature can occur. This additional observation strengthens our conclusion that the Γ-phase, and likely other intermetallic phases, form before cracking, because unconstrained growth of intermetallic phases in a crack cavity after cracking is not expected to yield the observed line defects. Instead, their presence suggests high local stresses. Whilst Fig. 2a exclusively shows cracking through intermetallics, other investigated locations also reveal cracking at the matrix-intermetallic interface.

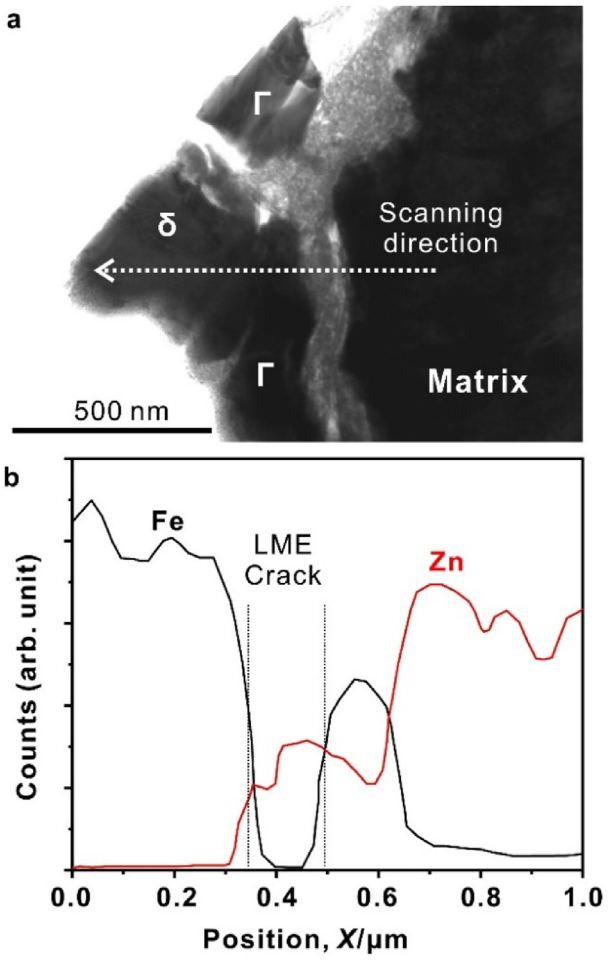

Fig. 3. TME-EDS analyzed cracked grain boundary. a) BF image of the crack path. The white dotted line indicates where the in b) displayed Fe and Zn concentration profiles have been measured.

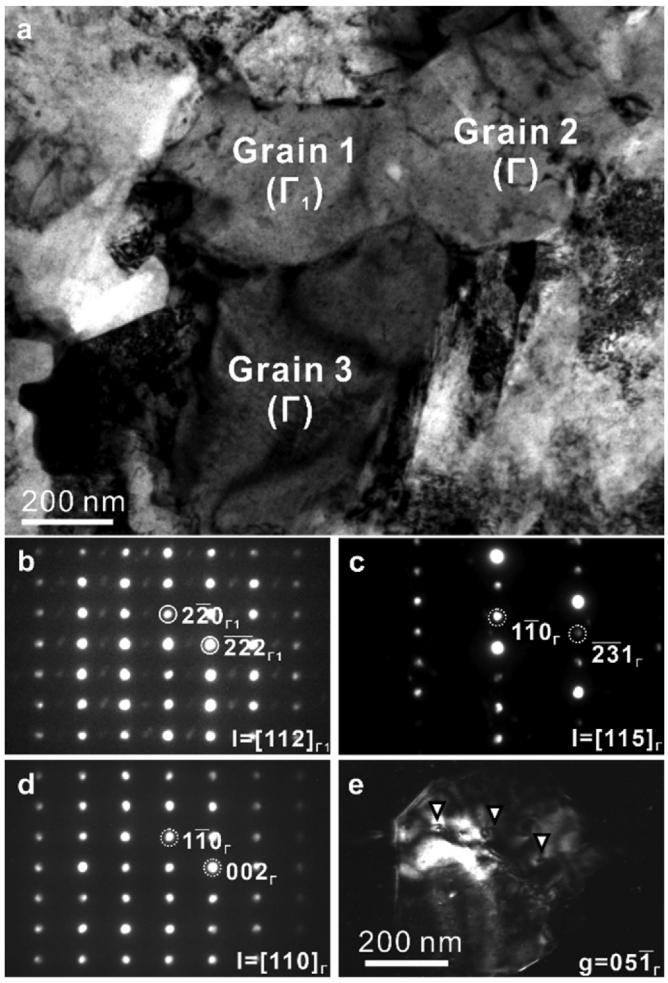

Fig. 4. TEM micrograph of a Zn-infiltrated but uncracked boundary. a) BF image showing the full development of intermetallic phases prior to cracking. b) and c,d) are SAD patterns of the Γ_1-, and Γ-phase, respectively. e) is a DF image of grain 2, in which positions of dislocations are indicated with arrows, suggesting plastic deformation of the Γ-phase.

Fig. 3a highlights this, where Fig. 3b shows a compositional profile (in arbitrary count units) recorded along the scanning direction from the steel matrix into the δ-phase, above which a Γ-phase was identified. Since it is very unlikely that cracking of a Zn-infiltrated grain-boundary is followed by Fe-Zn intermetallic phase formation on only one side of the crack, also this observation speaks for Zn-infiltration and the growth of intermetallic phases prior to any LME-cracking. As such, cracking seems to be occurring below 782 °C, which is the onset temperature for the Γ-phase during cooling in the Fe-Zn phase diagram. Intermetallic precipitation in the grain-boundary network prior to cracking can further be substantiated by the fact that intermetallic phases with grain sizes of a few hundred nanometers can be identified in the uncracked grain-boundary network of the AHSS. Fig. 4a represents such a case, where no cracking is observed but the Zn-infiltration has progressed sufficiently to allow the nucleation and growth of Fe-Zn intermetallics. Specifically, the grains seen in Fig. 4a are identified as are Γ_1 (grain 1) and Γ (grains 2 & 3) phases. The corresponding SAD patterns for both identified phases are displayed in Fig. 4b–d.

Similar to the cracked intermetallics depicted in Fig. 2a, dislocations are observed in all intermetallic grains 1–3 identified in Fig. 4a. This is demonstrated for grain 2 (Γ) in Fig. 4e, where arrows mark line defects, supporting the earlier made conclusion that significant stresses must be present during nucleation and growth of the Γ and Γ_1 phases. The consistent identification of both the Γ and Γ_1 phases at infiltrated and uncracked grain boundaries suggest that these phases form in the early stages of LME and that the δ or ζ phases are later products. This may not immediately be expected from the binary equilibrium phase diagram [42], which at the higher temperatures and with a high Zn-supply would favor both δ or ζ Fe-Zn phases. However, given that the amount of Zn is kinetically limited by the supply through grain-boundary (or bulk) diffusion that renders the local environment Fe-rich, nucleation of Γ Fe-Zn is plausible. Having now defined a scenario, in which the Γ (or Γ_1) would represent the first intermetallic phase to be nucleated in a Zn-enriched, but uncracked grain boundary, the next step is to locate such nanoscale phases in a Zn-rich boundary. To this end, we pursue analytical (S)TEM investigations on Zn-infiltrated and intact boundaries, including diffraction mapping to identify possible nano-crystalline intermetallics.

Fig. 5 displays such a Zn-infiltrated but uncracked grain boundary imaged with BF-TEM. This uncracked boundary is situated ahead of a Γ-phase at an LME-crack tip. Whilst not immediately discernible in the TEM micrograph in Fig. 5a, SAD allows identifying the indicated grain boundary. Chemical mapping shown in Fig. 5b reveals the presence of Zn along the uncracked boundary, extending well into the Γ-phase present at the crack tip located on the right-hand side of Fig. 5b. A line scan across the uncracked grain

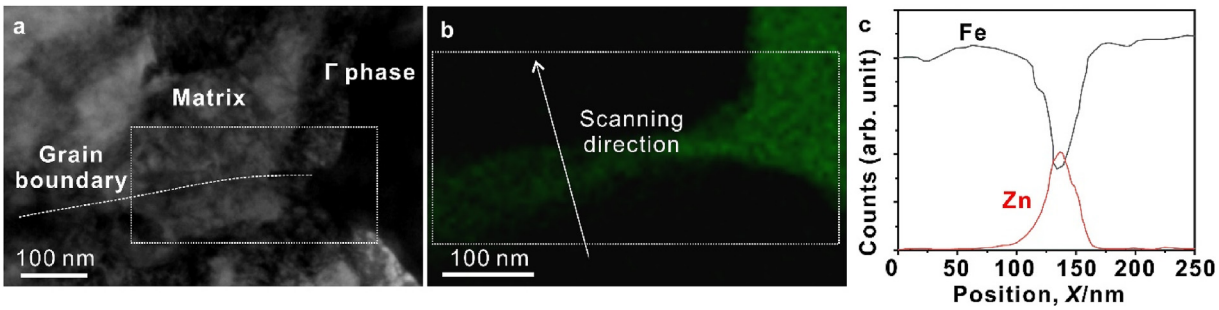

Fig. 5. TEM micrographs and elemental map of Zn in an uncracked boundary. a) BF image of a Zn-infiltrated grain boundary. The location of the grain boundary is indicated by a white dotted line. The elemental map in b) is obtained from the area indicated by the white rectangle in a). c) Line profiles of the Fe and Zn distribution across the uncracked boundary. The white arrow in b) indicates the EDS scanning path.

boundary is indicated and the corresponding concentration profiles for Fe and Zn are shown in arbitrary counts in Fig. 5c. The question at this point is if the Zn-infiltration in the uncracked boundary is elementary or if Fe-Zn intermetallic phases already have formed. To investigate this question, Scanning Electron Nano Diffraction (SEND also known as 4D STEM [43,44]) is conducted across the Zn-infiltrated interface.

Fig. 6a–c shows integrated diffraction patterns obtained with SEND for three different regions, being grain A (Fig. 6a), B (Fig. 6b), and the boundary (Fig. 6c) along the same uncracked grain boundary displayed in Fig. 5, but at a larger distance away from the Γ-phase (further to the right in Fig. 5a). The red arrow in Fig. 6c indicates a diffraction spot at a length of 3.9 nm^{-1} in reciprocal space (0.26 nm in real space), which is noticeable smaller than the shortest reciprocal vectors present in the diffraction patterns for the α- or γ-Fe phases (approximately 5 nm^{-1}). This suggests a diffraction contribution from a nanoscale intermetallic phase, the signal of which is very weak due to a small scattering volume and that furthermore is convoluted with the contributions from both grain A and B. In order to separate the different contributions and to eliminate multiple scattering effects, the diffraction patterns have been processed in the following way: (i) the intensities of the diffraction patterns are normalized from 0 to 1. (ii) The intensity contribution of the diffraction patterns from both grain A and B are subtracted from the pattern of boundary region (for brevity called 'C') in separate pairs (C-A and C-B). (iii) the images now containing difference intensities (C-A and C-B) are multiplied with each other, which strongly enhances the contribution from boundary region (C) in the finally obtained diffraction pattern, which is depicted in Fig. 6d. White arrows indicated in Fig. 6d now allow determining the underlying unit cell, which shows an excellent agreement with the Fe_3Zn_{10} Γ-phase.

This approach is subsequently used to construct a diffraction map across the uncracked boundary, which identifies the spatial distribution of the Fe_3Zn_{10} Γ-phase in the SEND mapped region. Fig. 6e reveals where the Γ-phase can be identified using the intensities of the diffraction spots. That means, brighter colors than blue map out the locations where a diffraction signal for the Γ-phase can be identified. These are primarily located along grain-boundaries that are indicated with solid lines. Here the grain boundaries have been located on the basis of diffraction spot intensity ratios from the different grains. Clearly, nanocrystals of the Γ-phase decorate the grain boundary, and the spatial deviation from the grain-boundary line is due to the fact that the grain boundary is not viewed edge on.

In addition to the spatial mapping of the intermetallic phase in the uncracked grain boundary, the SEND method allows quantifying an equivalent lattice strain based on the comparison of the spatially resolved diffraction data. This is done by using the standard lattice parameter for ferrite ($a_0 = 0.2866$ nm) as a reference. Here, we assume isotropic strain for three lattice translational vectors for simplicity. Given the reference value a_0 and the d spacing estimated from the length of corresponding g-vector in reciprocal space, $d_{hkl} = \frac{a}{\sqrt{h^2+k^2+l^2}}$ combined with $\varepsilon = \frac{a-a_0}{a_0}$, the equivalent strain is obtained as $\varepsilon = \frac{d_{hkl}\sqrt{h^2+k^2+l^2}}{a_0} - 1$. This equivalent strain is calculated using the shortest (or second shortest, if diffraction spots are very closely located) g-vector of the recorded diffraction patterns. Fig. 6f shows the distribution of this equivalent lattice strain across the areas of grain A and B, using the diffraction patterns of grain A. The reason for this extended area of grain A is the fact that the boundary between these two grains is not viewed edge on, resulting in sufficient diffraction spot intensity of grain A over the area of grain B. In other words, grain A overlaps with grain B in the projected view. Strong local fluctuations of primarily compressive equivalent lattice strains are seen across grain A, whereas local tensile components are located at the indicated approximate boundary line in Fig. 6e, where grains A and B overlap. We note that the spatial resolution of the used SEND method is ca. 1.8 nm, with a conservative equivalent strain precision of 0.2%, meaning that the fluctuations in Fig. 6f to h are significantly above the methods sensitivity. Fig. 6g displays the same data for grain B that does not further overlap with grain A above, which is the reason for the in gray shaded upper area. Thus, the overlap between grain A and B is below the boundary line indicated in Fig. 6e, thereby also defining its position. The strain fluctuations in grain B seen in Fig. 6g are significantly smaller and less heterogeneous than in grain A.

Merging the data in Fig. 6f and g generates the equivalent strain map for the entire region mapped with SEND, as shown in Fig. 6h. At this point, it has to be noted that there may be strain discontinuities across indicated boundaries, because the g-vectors used to derive the equivalent strain in each grain do not necessary align, meaning that different components of the here inaccessible strain tensor are probed. The composite view of all grains in Fig. 6h reveals that the largest strain variations are present along the boundary between grains A and B, as well as at the right side of grain B. The latter is in direct contact with a larger Γ-grains that is located ahead of the crack tip. We therefore conclude that this Γ-grain excerpts a compressive stress onto the adjacent ferrite grain (A), which is not surprising in view of volumetric increase of the intermetallic phase. The other regions where Γ-nanograins have been identified with SEND (Fig. 6e) do not always correspond directly to a local equivalent lattice strain heterogeneity. This is not surprising, because we are mapping a strain signature at room temperature after a complex thermo-mechanical process during which the Γ-nanograins formed. However, it is very apparent that

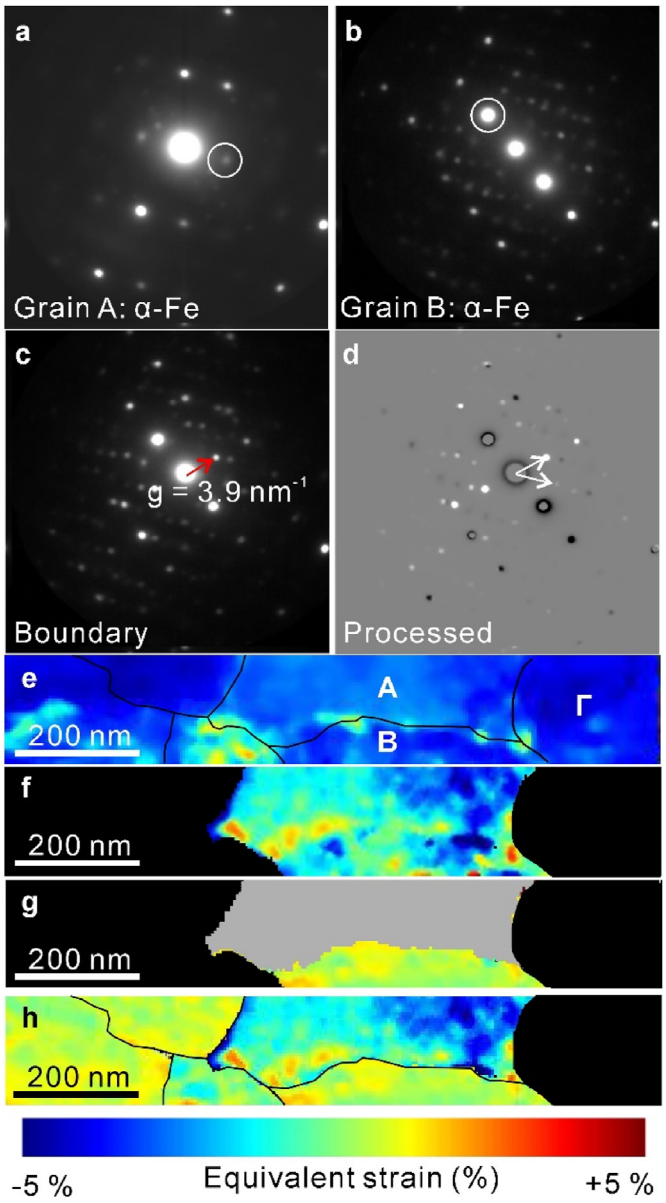

Fig. 6. Scanning electron nano diffraction data of a Zn infiltrated but uncracked boundary. a-c) show integrated diffraction patterns obtained from grains A, B, and the uncracked grain boundary, respectively. The diffraction spot of 3.9 nm^{-1} indicated by the red arrow in c) indicates the presence of a nanoscale Γ-phase, which was identified based on the processed diffraction pattern in d). e) represents the distribution of the nanoscale Γ-phase along the uncracked grain boundaries. f) and g) are the obtained strain distributions of grain A and B, respectively. h) shows the lattice strain map across all mapped grains. (For interpretation of the references to color in this figure legend, the reader is referred to the Web version of this article.)

the boundary between grain A and B, which according to Fig. 6e contains numerous Γ-nanograins, also displays distinctly enhanced fluctuations in local strain. This is not the case for the two grains located to the far left, where Γ-nanograins could not be revealed. We therefore deduce that the nucleation and growth of Γ-nanograins in Zn-infiltrated but uncracked grain boundaries are likely promoting local cracking. One consequently must consider intermetallic precipitation in the grain-boundary network, where depending on the local stress state, an LME crack connects local weak environments. This would explain why uncracked boundaries containing intermetallics can be found next to a crack (as in Fig. 1b), or why local cracks can be identified that are not directly connected

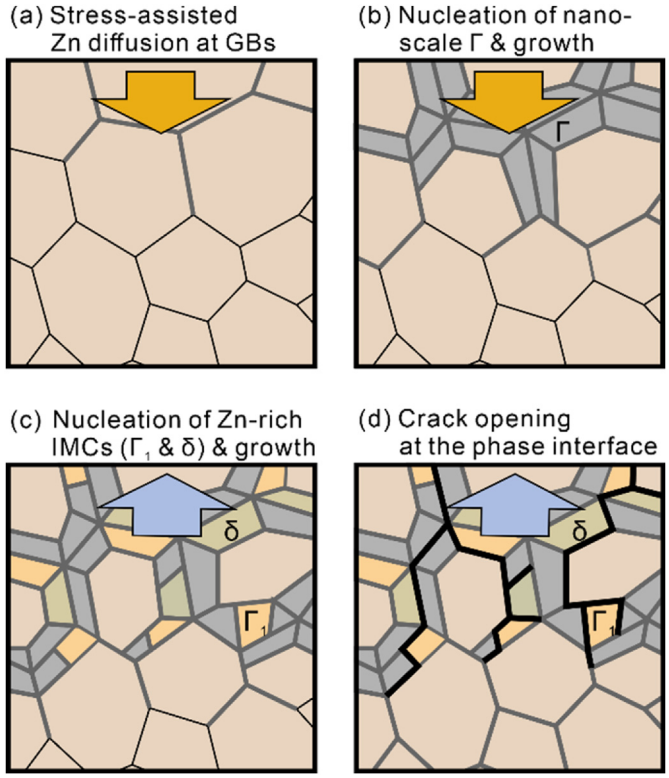

Fig. 7. Schematic of LME cracking based on the here obtained data. (a) Zn diffuses into grain boundaries via stress-assisted diffusion. (b) Impurity diffusion of Zn into the adjacent matrix occurs, followed by the nucleation and growth of initially the Γ-phase while maintaining a cube-on-cube orientation relationship. This step was here found to cause significant strain heterogeneities within the grain boundaries (c) Thermal stress developed between Fe-Zn intermetallic phases (IMCs) as well as between Fe-Zn IMCs and α-Fe during cooling down from the ductility trough. Zn-rich Fe-Zn phases form. (d) LME crack formation along the interfaces between IMCs or IMC phase and the matrix that subsequently are filled with liquid Zn.

to a main crack. However, this is difficult to unambiguously address, as all insights gained from the here used SEM- or TEM-based methods inherently are limited to a cross-sectional 2D view of a 3D grain-boundary network.

In concert, the findings included in Figs. 2–7 nurture the hypothesis that LME cracking in the studied AHSS proceeds by Zn diffusion into the grain-boundary network, followed by nucleation and growth of intermetallic Fe-Zn phases in the boundary, after which cracking occurs. We emphasize that a suite of previous studies has investigated LME cracking of galvanized AHSS and have concluded that intermetallic phase formation sets in after LME cracking [23–25,27]. In such a scenario, weakening would be dominated by chemical changes due to Zn diffusing into the boundary, whereas our observations clearly speak for nucleation and growth of intermetallic phases in the boundary that cause local stress heterogeneities. This is an important mechanistic difference and effectively places the critical part of the cracking mechanism to a temperature regime in which the intermetallic phases are stable (below 782 °C, 550 °C, and 672 °C for the Γ, Γ_1, and δ-phase, respectively). These temperatures remain above the melting temperature of pure Zn, but given the reducing solubility of Zn in ferrite with decreasing temperature, Zn supply to the grain boundary could also be ensured via the surrounding matrix.

In this context, it is instructive to simply consider the build-up of local stresses via volume expansion. Relative to α-iron, the Γ, Γ_1, and δ-phase have a 5.5%, 7.9%, and 8.0% lower density, respectively. In an idealized case, this can be represented by a spherical volume

expansion in an infinite interface that resembles a mode I crack geometry. These volumetric differences are significant and are expected to generate severe stress concentrations that may be more important than the much discussed far field thermo-mechanical stresses present during spot welding [8]. Prior to any formation of intermetallics and their phase transformations during cooling, Zn must, however, diffuse quickly into the grain-boundary network. As such, our work unambiguously supports embrittler transport via solid-state diffusion over liquid Zn flow [45]. This phase of the LME mechanism is hard to assess, but it has been suggested that the diffusivity of Zn in iron should be significantly enhanced by stress to achieve the large penetration depth [11,21,26]. Two scenarios are possible: 1) a fast Zn diffusion across the full crack length, and 2) a step-wise diffusion over a scale given by the length of the uncracked but infiltrated grain boundary. For the first case, a back-of-the-envelope estimate using the welding time (t = 400 ms) and a typical crack length (ca. 25 μm) returns a diffusion coefficient of at least 1.56×10^{-9} m^2/s that is several orders of magnitude larger than what the temperature range of the ductility trough (10^{-12}–10^{-11} m^2/s at 700-900 °C) would suggest, when considering grain boundary diffusion of Zn [46]. The second case of a step-wise progression assumes a repeating Zn infiltration and crack-opening, for which the diffusion distance would be much smaller. Here, we now assume that the total crack length X is met by n-times infiltration and abrupt cracking processes, over a total duration T. This can be expressed as $\frac{X}{n} = \sqrt{D\frac{T}{n}}$, leading to $D = \frac{X^2}{nT}$, suggesting that when the unit crack length becomes smaller, the necessary diffusion constant would be smaller as well. Given the reference grain boundary diffusion coefficient (10^{-12}–10^{-11} m^2/s at 700-900 °C), again the back-of-the-envelope estimate suggests that n ranges from approximately 156 to 1562. Therefore, the unit cracking length could be estimated as X/n, which corresponds to diffusion lengths between 160 nm−16 nm, respectively. This is far smaller than the infiltration length of Zn in the here studied uncracked grain boundaries. These simple thought experiments suggest that, in either case, stress-assisted grain boundary diffusion is key to explain the resulting crack length, underlining our current lack of understanding of how quick Zn transport can proceed in the ductility trough.

Based on our observations, we will now proceed with proposing a sequence of the LME-degradation process, according to the following steps that are schematically summarized in Fig. 7:

- Initially, Zn penetrates along high-angle random grain boundaries [12,20–22,33] via stress-assisted diffusion (Fig. 7a). The diffusivity was not quantitatively assessed here, but the presence of the embrittler far away from the crack in uncracked boundaries strongly supports a solid-state diffusion penetration of Zn.
- Nucleation, and possibly abrupt growth [47–49] of Fe-Zn-phases in the grain boundary. Due to the high Fe supply in the infiltrated boundaries, the Γ-phase forms first, which is further facilitated by a favorable lattice coherency (low nucleation barrier) with α-Fe (Fig. 7b).
- Crack-initiating local stress heterogeneities from the nucleation of Γ-FeZn may be amplified during cooling if the Γ-phase develops into the Γ_1 or the δ -phase through continued Zn supply. At the same time thermal stresses increase due to the large mismatches of thermal expansion coefficients between the various intermetallic and metal phases (Fig. 7c) [50,51].
- Microcracking at grain boundaries occurs at the interface between the intermetallic phases or between the intermetallic phases and the substrate (Fig. 7d).

This means that cracks connecting to the surface may again be filled with liquid Zn, which in turn would lead to the often reported fully Zn-filled cracks that were taken as evidence for that the intermetallic phases inside the cracks form as a result of a solidifying Fe-Zn-liquid [23–25]. However, this secondary infiltration is not the root cause of the initial failure mechanism but does provide continued supply of Zn for the surrounding grain-boundary network.

4. Concluding remarks

Our observations underline the need for focused nanoscale and atomic scale microstructural investigations that can pin down the sequence of events leading to macroscopic or mesoscopic LME-failure. Of particular focus should be the identification of a critical step, which we here propose being the formation and growth of Fe-Zn intermetallic phases in the infiltrated but uncracked grain-boundary network. The findings stand in some contrast to the recent observation of boundary weakening due to a change of the binding state of Fe due to Zn [22]. If this change in electronic structure due to pure chemical effects in the grain boundary would be the critical part of the failure mechanism, cracking would not proceed along phase or grain boundaries of intermetallic phases and their formation would indeed, as proposed in earlier more coarse-scale studies [23,24], first begin after decohesion of the boundary and subsequent infiltration of liquid Zn. This seems incompatible with the vast presence of uncracked environments containing intermetallics that only can form if sufficient Zn is present. Based on the here presented results, chemical effects that change the grain-boundary energy cannot be excluded, but at the same time Fe-rich intermetallic nanograins develop in the boundary prior to cracking, questioning the critical role of elementary Zn.

In summary, we provide strong evidence for that LME cracking of Zn-galvanized AHSS steel is driven by the nucleation and growth of Fe-Zn intermetallic phases. This insight is gained by studying the nanoscopic microstructural details of infiltrated, but uncracked grain boundaries. The presence of the here revealed nanoscale intermetallics that are embedded in the uncracked grain boundaries leads to stress heterogeneities due to volumetric differences, phase transformations during cooling, and mismatches in thermal expansion between the formed phases that eventually cause local microcracking. We therefore conclude that the observed formation of intermetallic phases is not a result of liquid Zn infiltration after cracking already has occurred. Instead, these intermetallic phases seem to represent a very early stage of LME degradation and therefore alloy-design strategies that limit Zn diffusion into the grain-boundary network or that suppress the nucleation and growth of intermetallic phases in the grain boundaries would be key to intrinsically mitigate LME degradation in future generation advanced high-strength steels.

Credit author statement

Y. Ikeda: Formal analysis, Investigation, Writing - Original Draft, Visualization **R. Yuan**: Softaware, Formal analysis, Investigation **A. Chakraborty**: Resources, Writing - Review & Editing **H. Ghassemi-Armaki**: Resources, Writing – Review & Editing **J.M. Zuo**: Supervision **R. Maaß**: Writing – Original Draft, Review & Editing, Supervision, Conceptualization, Resources, Funding acquisition.

Data availability

The raw/processed data required to reproduce these findings cannot be shared at this time as the data also forms part of an ongoing study.

Declaration of competing interest

The authors declare that they have no known competing financial interests or personal relationships that could have appeared to influence the work reported in this paper.

Acknowledgements

This research was carried out in part at the Frederick Seitz Materials Research Laboratory Central Research Facilities, University of Illinois. R.M. is grateful for financial support from ArcelorMittal, the Department of Materials Science and Engineering at UIUC, and the Federal Institute for Materials Research and Testing (BAM). Y.I. gratefully acknowledges the Takenaka Scholarship Foundation for their kind support of his graduate work.

References

[1] G. Meschut, C. Böhne, M. Rethmeier, M. Biegler, J. Frei, Combined Reports - AHSS Implementation Solutions: Liquid Metal Embrittlement Study, World Auto Steels, 2020.
[2] I.-J. Park, S.-M. Lee, M. Kang, S. Lee, Y.-K. Lee, Pitting corrosion behavior in advanced high strength steels, J. Alloys Compd. 619 (2015) 205–210.
[3] K. Han, I. Ohnuma, K. Okuda, R. Kainuma, Experimental determination of phase diagram in the Zn-Fe binary system, J. Alloys Compd. 737 (2018) 490–504.
[4] V. Raghavan, Fe-Zn (Iron-Zinc), J. Phase Equil. 24 (6) (2003) 544–545.
[5] Z. Ling, M. Wang, L. Kong, Liquid metal embrittlement of galvanized steels during industrial processing: a review, in: S. Chen, Y. Zhang, Z. Feng (Eds.), Transactions on Intelligent Welding Manufacturing, Springer Singapore, Singapore, 2018, pp. 25–42.
[6] D. Bhattacharya, Liquid metal embrittlement during resistance spot welding of Zn-coated high-strength steels, Mater. Sci. Technol. 34 (15) (2018) 1809–1829.
[7] M.H. Razmpoosh, C. DiGiovanni, Y.N. Zhou, E. Biro, Pathway to understand liquid metal embrittlement (LME) in Fe-Zn couple: from fundamentals toward application, Prog. Mater. Sci. (2021), 100798.
[8] Z. Ling, M. Wang, L. Kong, K. Chen, Towards an explanation of liquid metal embrittlement cracking in resistance spot welding of dissimilar steels, Mater. Des. 195 (2020), 109055.
[9] J. Geunsu, Zn-assisted Liquid Metal Embrittlement of High Mn Austenitic Steels, Doctoral Dissertation, 2015.
[10] J. Van den Bosch, G. Coen, P. Hosemann, S.A. Maloy, On the LME susceptibility of Si enriched steels, J. Nucl. Mater. 429 (1–3) (2012) 105–112.
[11] H. Kang, L. Cho, C. Lee, B.C. De Cooman, Zn penetration in liquid metal embrittled TWIP steel, Metall. Mater. Trans. 47 (6) (2016) 2885–2905.
[12] S. American Welding, M. Tumuluru, Effect of silicon and retained austenite on the liquid metal embrittlement cracking behavior of GEN3 and high-strength automotive steels, WJ 98 (12) (2019) 351–364.
[13] K. Wolski, N. Marié, M. Biscondi, AES quantification of intergranular film thickness in the Ni-Bi system with respect to the liquid metal embrittlement phenomenon, Surf. Interface Anal. 31 (4) (2001) 280–286.
[14] R.C. Hugo, R.G. Hoagland, In-situ TEM observation of aluminum embrittlement by liquid gallium, Scripta Mater. 38 (3) (1998) 523–529.
[15] R.C. Hugo, R.G. Hoagland, Gallium penetration of aluminum: in-situ TEM observations at the penetration front, Scripta Mater. 41 (12) (1999) 1341–1346.
[16] M. Naderi, M. Peterlechner, E. Schafler, S.V. Divinski, G. Wilde, Kinetic, volumetric and structural effects induced by liquid Ga penetration into ultrafine grained Al, Acta Mater. 99 (2015) 196–205.
[17] L. Ren, D.F. Bahr, R.G. Hoagland, Influence of grain boundary structure on liquid metal penetration behavior, MRS Proc 578 (1999) 411–486.
[18] R. Case, D.R. McIntyre, Mercury liquid metal embrittlement of alloys for oil and gas production and processing, in: NACE International Corrosion 2010 Conference & Expo, 2010, pp. 1–10.
[19] H. Lu, Y. Su, Y. Wang, W. Chu, In situ TEM research of dislocation emission and microcrack nucleation for Ti after adsorption by Hg, Corrosion Sci. 41 (4) (1999) 699–708.
[20] M.H. Razmpoosh, A. Macwan, F. Goodwin, E. Biro, Y. Zhou, Role of random and coincidence site lattice grain boundaries in liquid metal embrittlement of Iron (FCC)-Zn couple, Metall. Mater. Trans. 51 (8) (2020) 3938–3944.
[21] M.H. Razmpoosh, E. Biro, D.L. Chen, F. Goodwin, Y. Zhou, Liquid metal embrittlement in laser lap joining of TWIP and medium-manganese TRIP steel: the role of stress and grain boundaries, Mater. Char. 145 (2018) 627–633.
[22] M.H. Razmpoosh, B. Langelier, E. Marzbanrad, H.S. Zurob, N. Zhou, E. Biro, Atomic-scale investigation of liquid-metal-embrittlement crack-path: revealing mechanism and role of grain boundary chemistry, Acta Mater. 204 (2021), 116519.
[23] H. Lee, M.C. Jo, S.S. Sohn, S.-H. Kim, T. Song, S.-K. Kim, H.S. Kim, N.J. Kim, S. Lee, Microstructural evolution of liquid metal embrittlement in resistance-spot-welded galvanized TWinning-Induced Plasticity (TWIP) steel sheets, Mater. Char. 147 (2019) 233–241.
[24] Z. Ling, T. Chen, L. Kong, M. Wang, H. Pan, M. Lei, Liquid metal embrittlement cracking during resistance spot welding of galvanized Q&P980 steel, Metall. Mater. Trans. 50 (11) (2019) 5128–5142.
[25] L. Cho, H. Kang, C. Lee, B.C. De Cooman, Microstructure of liquid metal embrittlement cracks on Zn-coated 22MnB5 press-hardened steel, Scripta Mater. 90–91 (2014) 25–28.
[26] L. Klinger, E. Rabkin, The effect of stress on grain boundary interdiffusion in a semi-infinite bicrystal, Acta Mater. 55 (14) (2007) 4689–4698.
[27] S.-H. Hong, J.-H. Kang, D. Kim, S.-J. Kim, Si effect on Zn-assisted liquid metal embrittlement in Zn-coated TWIP steels: importance of Fe-Zn alloying reaction, Surf. Coating. Technol. 393 (2020), 125809.
[28] J.R. Rice, J.-S. Wang, Embrittlement of interfaces by solute segregation, Mater. Sci. Eng., A 107 (1989) 23–40.
[29] J.D. McKinley, J.E. Vance, The vapor pressure of zinc between 150°C and 350°C, J. Chem. Phys. 22 (6) (1954) 1120–1124.
[30] I.O. Yilmaz, A.Y. Bilici, H. Aydin, Resistance spot weldability of TBF steel sheets with dissimilar thickness, Metall. Res. Technol. 117 (6) (2020).
[31] O. Siar, Y. Benlatreche, T. Dupuy, S. Dancette, D. Fabrègue, Effect of severe welding conditions on liquid metal embrittlement of a 3rd-generation advanced high-strength steel, Metals 10 (9) (2020) 1–11.
[32] S.P. Murugan, K. Mahmud, C. Ji, I. Jo, Y.D. Park, Critical design parameters of the electrode for liquid metal embrittlement cracking in resistance spot welding, Weld. World 63 (6) (2019) 1613–1632.
[33] M.H. Razmpoosh, A. Macwan, F. Goodwin, E. Biro, Y. Zhou, Crystallographic study of liquid-metal-embrittlement crack path, Mater. Lett. 267 (2020), 127511.
[34] SEP 1220-2:2011-08, Testing and Documentation Guideline for the Joinability of Thin Sheet of Steel - Part 2: Resistance Spot Welding.
[35] C.H.E. Belin, R.C.H. Belin, Synthesis and crystal structure determinations in the Γ and δ phase domains of the Iron–Zinc system: electronic and bonding analysis of Fe13Zn39 and FeZn10, a subtle deviation from the Hume–Rothery standard? J. Solid State Chem. 151 (1) (2000) 85–95.
[36] A.S. Koster, J.C. Schoone, Structure of the cubic iron–zinc phase Fe22Zn78, Acta Crystallogr. B Struct. Crystallogr. Cryst. Chem. 37 (10) (1981) 1905–1907.
[37] M.H. Hong, H. Saka, Transmission electron microscopy of the iron-zinc delta1 intermetallic phase, Scripta Mater. 36 (12) (1997) 1423–1429.
[38] K.-K. Wang, C.-W. Hsu, L. Chang, D. Gan, L.-J. Chiang, Formation of Fe-Zn intermetallic phases in Galvannealed Mn-Si TRIP steels, in: AIST Galvatech 2015 10th International Conference on Zinc and Zinc Alloy Coated Steel, 2015, pp. 81–87.
[39] X. Hu, T. Watanabe, Relationship between the crystallographic structure of electroplated Fe-Zn Alloy film and its thermal equilibrium diagram, J. Jpn Inst. Metal 64 (4) (2000) 234–241.
[40] H. Inui, N.L. Okamoto, S. Yamaguchi, Crystal structures and mechanical properties of Fe–Zn intermetallic compounds formed in the coating layer of Galvannealed steels, ISIJ Int. 58 (9) (2018) 1550–1561.
[41] M.H. Hong, H. Saka, The mechanical properties and dislocation structure of the Γ intermetallic phase in the Fe-Zn system, Philos. Mag. A 74 (2) (1996) 509–524.
[42] L. Zhu, S. Honrao, B. Rijal, R.G. Hennig, M.V. Manuel, Phase equilibria and diffusion coefficients in the Fe-Zn binary system, Mater. Des. 188 (2020), 108437.
[43] C. Ophus, Four-dimensional scanning transmission electron microscopy (4D-STEM): from scanning nanodiffraction to ptychography and beyond, Microsc. Microanal. 25 (3) (2019) 563–582.
[44] R. Yuan, J. Zhang, J.-M. Zuo, Lattice strain mapping using circular Hough transform for electron diffraction disk detection, Ultramicroscopy 207 (2019), 112837.
[45] C. DiGiovanni, A.G. Kalashami, E. Biro, N.Y. Zhou, Liquid metal embrittlement transport mechanism in the Fe/Zn system: stress-assisted diffusion, Materialia (2021), 101153.
[46] J.S. Dohie, J.R. Cahoon, W.F. Caley, The grain-boundary diffusion of Zn in α-Fe, J. Phase Equilibria Diffus. 28 (4) (2007) 322–327.
[47] C.E. Jordan, A.R. Marder, Effect of substrate grain size on iron-zinc reaction kinetics during hot-dip galvanizing, Metall. Mater. Trans. 28 (12) (1997) 2683–2694.
[48] J.D. Culcasi, P.R. Seré, C.I. Elsner, A.R. Di Sarli, Control of the growth of zinc–iron phases in the hot-dip galvanizing process, Surf. Coating. Technol. 122 (1) (1999) 21–23.
[49] J. Inagaki, M. Sakurai, T. Watanabe, Alloying reactions in hot dip galvanizing and galvannealing processes, ISIJ Int. 35 (11) (1995) 1388–1393.
[50] A.T. Alpas, J. Inagaki, Effect of microstructure on fracture mechanisms in Galvannealed coatings, ISIJ Int. 40 (2) (2000) 172–181.
[51] A. Iost, J. Foct, Toughness and residual stresses in galvanizing coatings, J. Mater. Sci. Lett. 12 (17) (1993) 1340–1343.